



This is a repository copy of *Using shock control bumps to improve transonic fan/compressor blade performance*.

White Rose Research Online URL for this paper:
<http://eprints.whiterose.ac.uk/142878/>

Version: Accepted Version

Article:

John, A., Qin, N. and Shahpar, S. (2019) Using shock control bumps to improve transonic fan/compressor blade performance. *Journal of Turbomachinery*, 141 (8). 081003. ISSN 0889-504X

<https://doi.org/10.1115/1.4042891>

© 2019 ASME. This is an author produced version of a paper subsequently published in *Journal of Turbomachinery*. Uploaded in accordance with the publisher's self-archiving policy. Article available under the terms of the Creative Commons Attribution Licence (<http://creativecommons.org/licenses/by/4.0>)

Reuse

This article is distributed under the terms of the Creative Commons Attribution (CC BY) licence. This licence allows you to distribute, remix, tweak, and build upon the work, even commercially, as long as you credit the authors for the original work. More information and the full terms of the licence here:
<https://creativecommons.org/licenses/>

Takedown

If you consider content in White Rose Research Online to be in breach of UK law, please notify us by emailing eprints@whiterose.ac.uk including the URL of the record and the reason for the withdrawal request.



eprints@whiterose.ac.uk
<https://eprints.whiterose.ac.uk/>

GT2018-77065

USING SHOCK CONTROL BUMPS TO IMPROVE TRANSONIC FAN/COMPRESSOR BLADE PERFORMANCE

Alistair John
University of Sheffield
Sheffield, S1 3JD
United Kingdom
adjohn1@sheffield.ac.uk

Ning Qin
University of Sheffield
Sheffield, S1 3JD
United Kingdom

Shahrokh Shahpar
Rolls-Royce
Derby, DE24 8BJ
United Kingdom

ABSTRACT

Shock control bumps can help to delay and weaken shocks, reducing loss generation and shock-induced separation and delaying stall inception for transonic turbomachinery components. The use of shock control bumps on turbomachinery blades is investigated here for the first time using 3D analysis. The aerodynamic optimisation of a modern research fan blade and a highly loaded compressor blade are carried out using shock control bumps to improve their performance. Both the efficiency and stall margin of transonic fan and compressor blades may be increased through the addition of shock control bumps to the geometry. It is shown how shock induced separation can be delayed and reduced for both cases. A significant efficiency improvement is shown for the compressor blade across its characteristic, and the stall margin of the fan blade is increased by designing bumps that reduce shock-induced separation near to stall. Adjoint surface sensitivities are used to highlight the critical regions of the blade geometries, and it is shown how adding bumps in these regions improves blade performance. Finally, the performance of the optimised geometries at conditions away from where they are designed is analysed in detail.

NOMENCLATURE

CFD Computational Fluid Dynamics
LE Leading Edge
MAM Multi-point Approximation Method
PR Pressure Ratio

RANS Reynolds Averaged Navier Stokes
TE Trailing Edge

INTRODUCTION

Motivation

Shocks are a major source of loss for transonic fans and compressors. They cause entropy generation, boundary layer thickening and shock induced separation. The impingement of the shock on the blade suction surface (and the resulting, strong, adverse pressure gradient) can cause the boundary layer to detach, leading to larger blade wakes, reduced efficiency, lower blade stability and reduced stall margin. Any method that can be used to alleviate shock strength (and the associated negative effects) therefore has the potential to significantly improve transonic fan/compressor performance.

Shock control for turbomachinery

Relatively little work on designing geometries directly to weaken the shock waves in transonic turbomachinery components can be found in the literature, though it has been known for some time that reducing the pre-shock Mach number of transonic compressors can improve their efficiency [1].

It was clear to transonic compressor designers in the 70s and 80s that shock strength was increased by the amount of convex curvature on the suction side between the leading edge and the shock [2]. Nearly flat suction surfaces that minimised the expansion were therefore favoured, with the next step to try designs

the NASA rotor 67 geometry.

They added a bump modelled using the Hicks–Henne function [13]. It was shown how the interaction of the bump with the original wave structure resulted in a more desirable pressure gradient, with a weaker compression wave fan and a more isentropic compression field. The bump design was optimised and was shown to reduce the separation area at an off-design condition. They describe how this may have the potential to improve the stall properties of the blade section. Two optimisations were carried out, one at the design condition and another at 4% higher rotational speed. Optimal bumps were produced for each condition, with an increase in efficiency of 0.67% for the on-design case and 2.9% in the off design case reported. The optimised geometry for the design condition is shown in Figure 3.

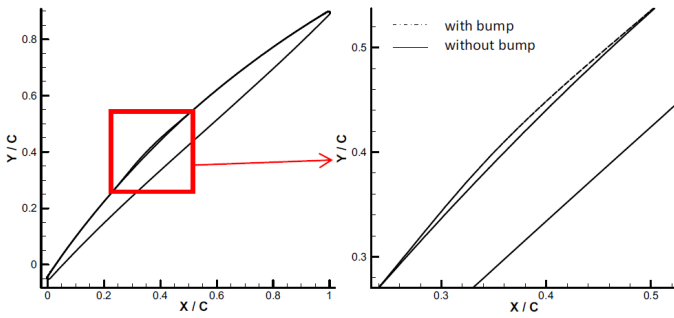


FIGURE 3: DATUM GEOMETRY AND OPTIMISED SHOCK CONTROL BUMPS ON THE MID SECTION OF NASA ROTOR 67. FROM MAZAHERI ET AL. [12].

The work by Mazaheri and Khatibirad demonstrated the benefit that bumps may provide at both on and off-design conditions, and their potential to improve stall margin. The simplified 2D analysis lacks accuracy however as the complex behaviour of radial and separated flow cannot be predicted. For a thorough understanding of the potential for the use of shock control bumps, 3D analysis and the design of 3D bumps is needed to truly assess their effect. This is carried out here.

CASES UNDER INVESTIGATION

Two cases are investigated in this work; firstly, the transonic compressor blade NASA Rotor 37, and secondly, a modern, low speed, transonic Rolls-Royce research fan blade (known here as RR-FAN). The impact of shock control bumps on both blade efficiency and stall margin is investigated.

1st case: NASA Rotor 37

The case first case studied here is NASA Rotor 37 [14]. This has a very strong shock wave (with a relative tip Mach number of nearly 1.5) which causes large separation, decreasing the blade efficiency. It is a well-documented case, having been extensively tested [15] [16] and simulated as part of a turbomachinery validation study [15] [17] [16] [18]. It is a transonic rotor with inlet hub-to-tip ratio 0.7, blade aspect ratio 1.19, rotor tip relative inlet Mach number 1.48 and rotor tip solidity 1.29. It has historically been a challenge for CFD simulation. The very high pressure ratio, strong shock wave-boundary layer interaction, large tip-leakage vortex and highly separated flow mean that it poses challenges for turbomachinery solvers. Rotor 37 has been the subject of review articles that highlight the complexity of matching experimental and computational measurements and the associated uncertainties [19] [20] [21].

The CFD setup is shown in Figure 4. At the inlet, a radial distribution of total pressure and temperature (based on the original experimental values [17]) is specified. The inlet turbulence intensity is 1%. At the outlet, a value for circumferentially mixed-out and radially mass-measured capacity (non-dimensional mass flow) is used. Periodic boundaries are used to represent full annulus flow. Stationary walls are treated as adiabatic viscous walls and the rotational speed of the non-stationary portions of the domain is $1800.01 \text{ rad s}^{-1}$, as specified in the experiment. Rolls-Royce CFD solver Hydra [22] is used for all of the simulations presented here, using the Spalart-Allmaras turbulence model (fully turbulent). The 4.27 million cell mesh is generated by PADRAM [23], has y^+ of the order of one on all surfaces with 30 cells in the tip gap. Mesh independence is shown in Figure 5. Images of the mesh can be found in [4].

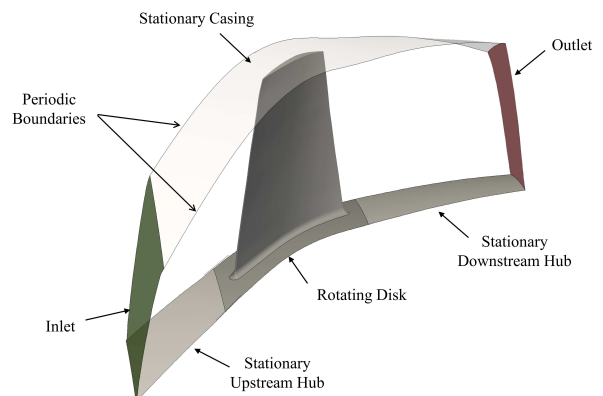


FIGURE 4: THE R37 CFD DOMAIN USED.

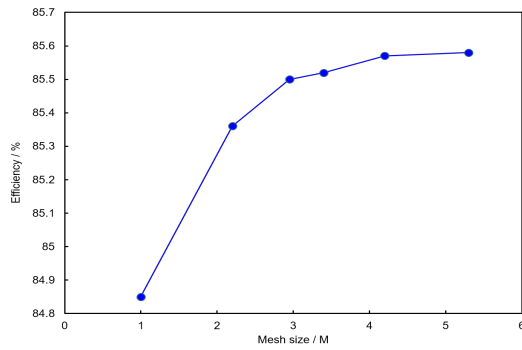


FIGURE 5: MESH INDEPENDENCE FOR R37 BLADE.

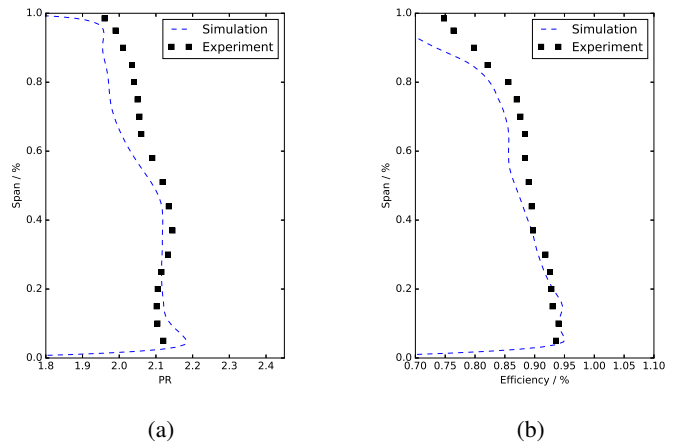


FIGURE 7: RADIAL PROFILES VS EXPERIMENTAL DATA.

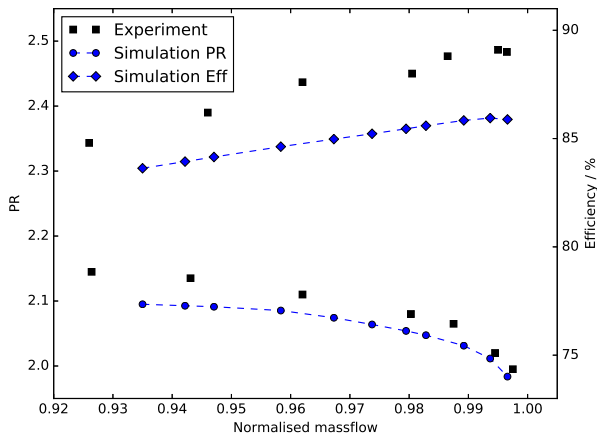


FIGURE 6: SIMULATED CHARACTERISTICS VS EXPERIMENTAL DATA. [15]

Validation

As previously alluded to, many studies have struggled when matching simulations of Rotor 37 to the experiment. A wide range of work has been undertaken to investigate the discrepancy found between simulation and experiment, with the primary work being the 1994 ASME/IGTI blind test case study in which a range of codes were used to simulate the rotor, with no knowledge of the experimental values. A large variation was seen between the different predictions, prompting analysis by Denton [19]. Recent work has also been carried out by Chima [18] and Hah [16]. The differences are usually attributed to uncertainty in the experimental measurements, the lack of real geometry in the simulations (e.g. the upstream hub cavity is usually missing) [21] and also the difficulty in fully resolving the complex flows. Figures 6 and 7 show comparisons of the current simulation results versus the experiment.

The pressure ratio agreement is reasonable across the char-

acteristic, but the efficiency prediction is about 2% below the experimental value at the design point (98% choke). This matches the trend of previous results, where the better the PR prediction, the worse the efficiency match. This 'trade-off' has been seen in a range of previous simulations [17].

Figure 7 gives the radial profiles of total PR and efficiency at 98% of simulated choke compared to the experimental values at 98% experimental choke. The radial trends have been captured fairly well, although there is an offset from the experiment for both. The choke mass flow found in the simulations was 20.91kgs^{-1} , matching quite closely the experimental of 20.93kgs^{-1} .

Flow field for the datum case

Figure 8 shows the flow features of the datum NASA Rotor 37 at design point. It can be seen how the strong shock of Rotor 37 causes complex shock-boundary layer interaction and a large shock-induced separation (this can be seen by the thickening of the boundary layer and wake shown in Figure 8b and the orange contour of zero axial velocity in Figure 8a). At the point where the shock impinges on the suction surface, its interaction with the boundary layer causes it to separate and a large wake forms. It is at this design point that Rotor 37 will be optimised, as a reduction in this separation could significantly increase blade efficiency.

2nd case: RR-FAN

The research fan blade used in this investigation is known as RR-FAN. It is a high bypass ratio, low speed Rolls-Royce fan blade. The relative Mach number at the tip is 1.07 and the chord-based Reynolds number is 3.6 million.

The blade is simulated in rotor only format, with a downstream splitter geometry and separate exit boundaries for the core

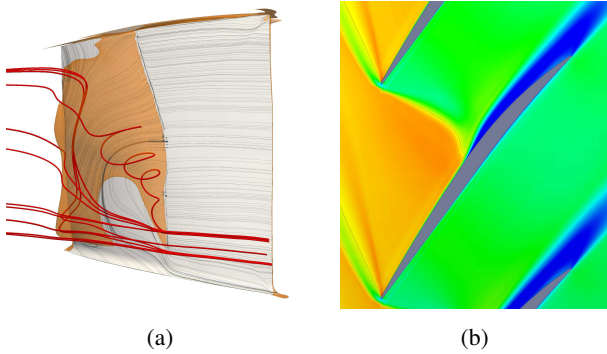


FIGURE 8: (a) 3D SEPARATION (ORANGE) ON THE R37 GEOMETRY (FLOW RIGHT TO LEFT), (b) REL. MACH NO. CONTOUR AT 60% SPAN.

and bypass flows. An outline of the CFD domain is shown in Figure 10. At the inlet, a radial distribution of total pressure and temperature is used and at the exit boundaries radially averaged mass-meant non-dimensionalised flow rate (capacity) is specified.

Mesh independence is shown in Figure 9. The mesh used is a high quality, 4.4M. multi-block PADRAM mesh. There are 30 cells in the tip clearance and the y^+ on all surfaces is of the order of one. The mesh is not shown here but examples of the same mesh used for a related blade are given in [24].

Validation

Due to experimental data for this geometry not being available, simulation validation was carried out using a similar fan blade geometry that has experimental data available. The related blade has very similar performance parameters, and the simulation set up is identical. The results are given here.

A comparison of the simulations of this related blade against experimental data can be seen in Figures 11 and 12. Both the pressure ratio and efficiency curves match the experimental data well, though there is a slight offset to the overall values and stall margin. The radial curves show good comparison to experimental data, although the radial variation in efficiency is under-predicted compared to the experiment. Overall, the simulation compares well, lying within 1% across the range of flow rates.

Blade flow features

To understand the behaviour of this blade design and select a point at which to optimise the geometry, the flow behaviour for a range of flow rates was studied (see Figures 13 and 15).

Figure 15 shows the flow features of the blade design as the flow rate is varied (as shown in Figure 13). Point A is stalled. For proprietary reasons the whole RR-FAN blade geometry cannot be shown, hence, flow behaviour in just the region of interest is

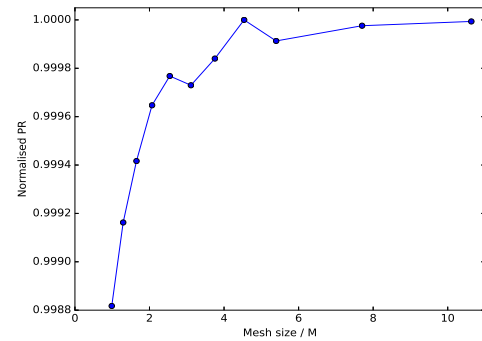


FIGURE 9: MESH INDEPENDENCE FOR THE RR-FAN BLADE.

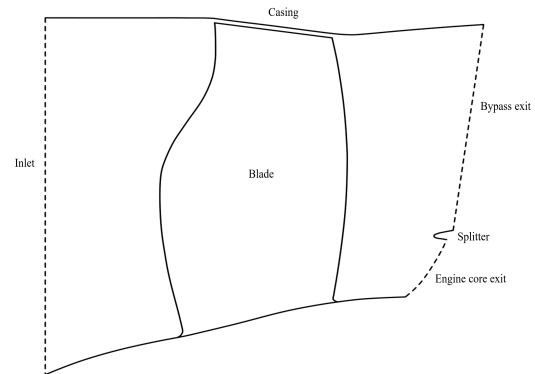


FIGURE 10: THE CFD DOMAIN USED FOR RR-FAN (NOT REPRESENTATIVE OF THE ACTUAL FAN GEOMETRY)].

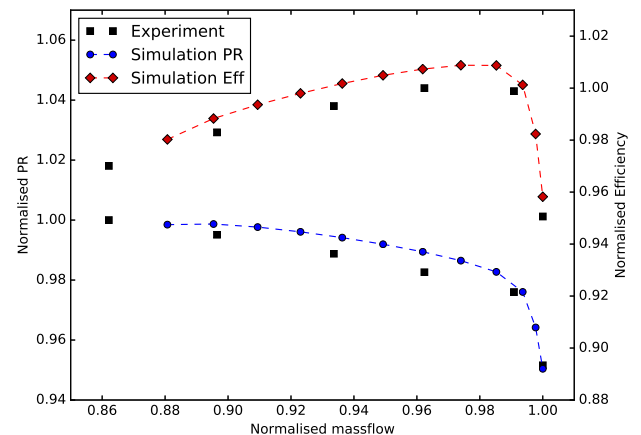


FIGURE 11: COMPARISON OF THE SIMULATION RESULTS FOR THE RR-FAN RELATED BLADE WITH EXPERIMENTAL DATA.

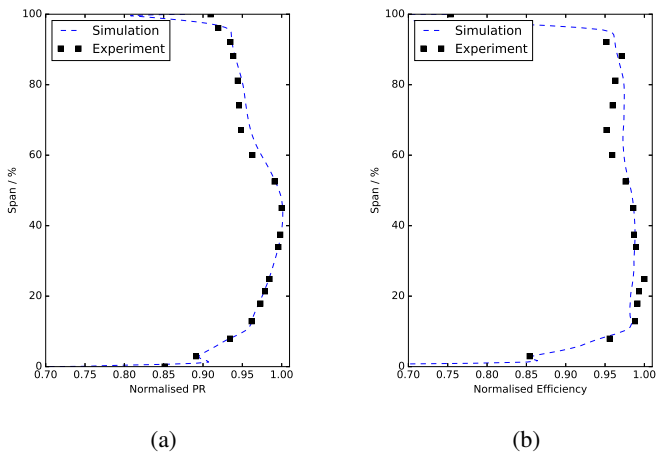


FIGURE 12: RADIAL PROFILES FOR THE RR-FAN RELATED BLADE AT DESIGN POINT (a) PR, (b) EFFICIENCY.

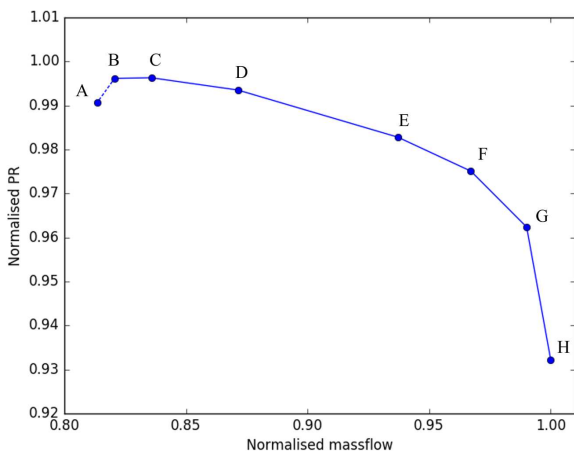


FIGURE 13: RR-FAN PR CHARACTERISTIC OPERATING POINTS.

shown in the following figures. Figure 14 describes this region of interest.

The shock position on the blade surface moves towards the LE as the operating point moves to the left on the characteristic. As the pressure ratio increases and flow rate becomes lower, the strength of the shock increases and separation is caused towards stall. It is this separation (highlighted in orange) that contributes to the full stall of the blade. It can be seen that the shock-induced separation increases in magnitude and radial extent as the flow rate is lowered until full separation eventually occurs.

These near-stall operating points are a promising area to investigate the benefit of shock control bumps. It is the shock-

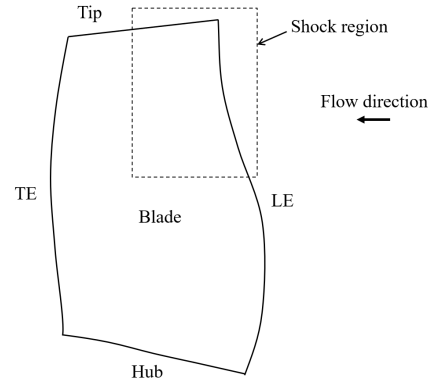


FIGURE 14: THE REGION OF INTEREST (SHOCK REGION) PRESENTED IN FURTHER RR-FAN FIGURES (NOT REPRESENTATIVE OF THE ACTUAL FAN GEOMETRY).

induced separation that is responsible for limiting the operating range of the blade, and if this separation can be reduced then it is expected that this will extend the stable working range of this fan.

Adjoint sensitivity analysis

Adjoint sensitivity analysis is a useful tool that can be used to provide information on the sensitivity of an objective function to changes in the geometry. Here, the adjoint sensitivity used is the sensitivity of efficiency (as a percentage) to surface deformation (in mm) normal to the surface. This can be used to inform which regions of the blade will have the greatest impact when modified, and are therefore most important to control during an optimisation. Hydra Adjoint [25] is used to provide the blade surface sensitivities: A primal Hydra simulation is first used to provide the flow solution, followed by Hydra adjoint which calculates the flow-adjoint sensitivity and provides the sensitivity of the objective function to changes in the flow. Once these two relatively expensive simulations are completed, the mesh sensitivities are then mapped onto the surface. This finds the relationship between changes in the flow to changes in the blade surface mesh. Combining these provides the sensitivity (gradient) of the objective function (efficiency) to perturbations of the blade surface.

The adjoint surface sensitivity analysis for Rotor 37 at design point and RR-FAN at point D (see Figure 13) are given in Figures 16 and 17. It can be seen that the most sensitive regions of both geometries are focussed around the shock on the suction surface. This indicates that geometry changes in this region will have a significant impact on the blade efficiency, and therefore if shock control bumps are applied here some benefit should be

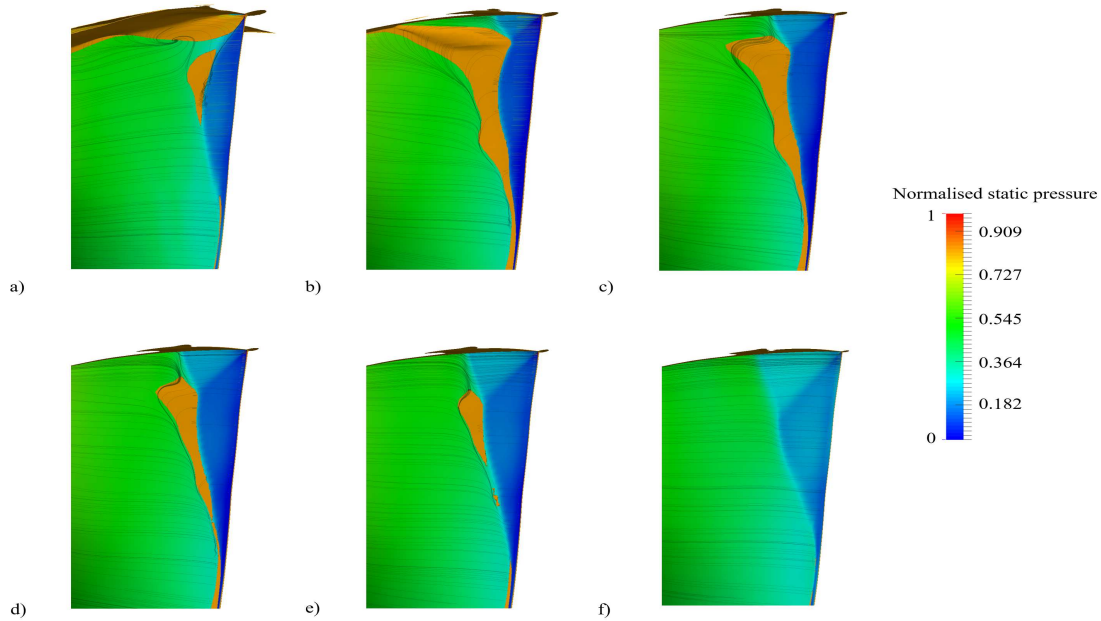


FIGURE 15: SHOCK REGION FLOW FEATURES FOR RR-FAN AT POINTS a) A, b) B, c) C, d) D, e) E, f) F. FLOW DIRECTION RIGHT TO LEFT.

found.

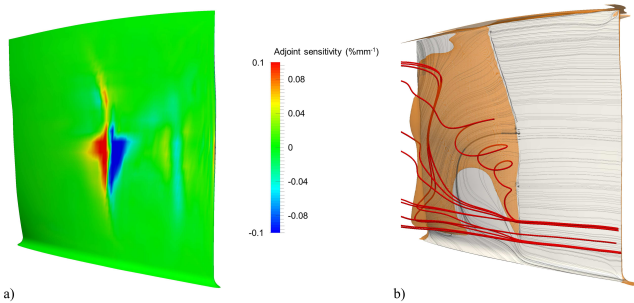


FIGURE 16: R37 (a) ADJOINT SENSITIVITY AND (b) 3D STREAMLINES (RED) AND REVERSE FLOW (ORANGE). FLOW DIRECTION RIGHT TO LEFT.

SHOCK BUMP PARAMETERISATION AND OPTIMISATION

The CST (Class Shape Transformation) method [26] is used in this work to define the bump geometries. The CST method uses Bernstein polynomials to create smooth (second deriva-

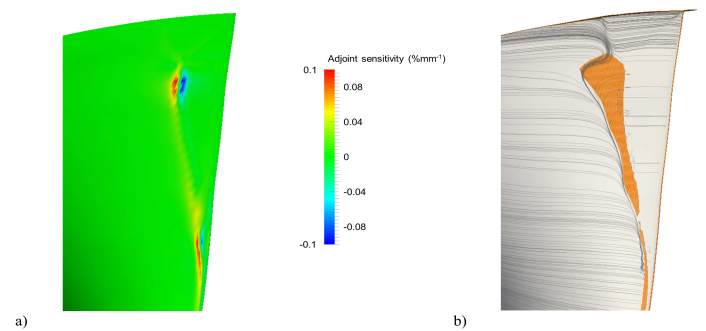


FIGURE 17: RR-FAN (a) SHOCK REGION ADJOINT SURFACE SENSITIVITY AND (b) FLOW SEPARATION NEAR TO STALL (POINT D). FLOW DIRECTION RIGHT TO LEFT.

tive continuous) contour bumps. For this project 3rd order CST bumps are used, constructed from four Bernstein polynomials. Controlling the weighting (amplitude) of these polynomials modifies the bump height and asymmetry. Figure 18 shows how the bump geometry (solid black line) to be added to the blade surface is a sum of the four Bernstein polynomials (coloured dashed lines). The CST bump parameterisation provides a high degree of flexibility, enabling the generation of smooth, asymmetric bumps in 2D and 3D.

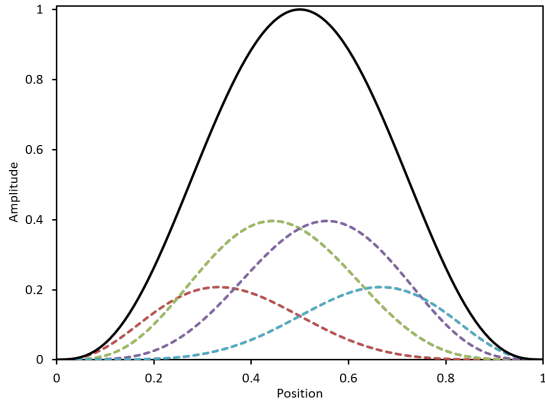


FIGURE 18: EXAMPLE 2D CST BUMP (SOLID LINE) AND THE FOUR POLYNOMIALS USED TO CONSTRUCT IT (DASHED LINES).

The CST bump parameterisation technique was implemented inside of the PADRAM [23] geometry and meshing software. The technique modifies each 2D radial section of the blade geometry, adding a bump. The properties of these 2D bumps are smoothly interpolated in the radial direction from control sections. The resulting geometry is controlled by the bump start and end positions, the four Bernstein polynomial amplitudes and the span-wise distribution. This allows 3D variation of the bumps in the radial direction.

Both continuous (where bump amplitudes are smoothly interpolated radially) and individual (where the bump amplitude returns to zero periodically in the radial direction) CST bumps were tested. Examples of the blade with individual and continuous bumps added is shown in Figure 19.

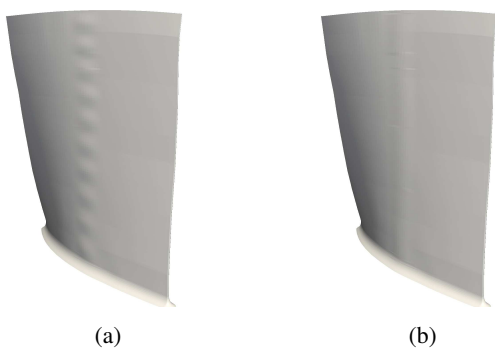


FIGURE 19: a) EXAMPLE INDIVIDUAL BUMP GEOMETRY AND b) EXAMPLE CONTINUOUS BUMP GEOMETRY

During this work, a study was carried out (not detailed here for brevity) to compare the benefit of using individual bumps

(where a series of discrete bumps is added to the datum geometry in the radial direction) with a continuous bump (note continuous bumps are still '3D' and their shape, position and amplitude can vary in the radial direction). It was concluded that, for these cases, the individual bumps needed to have greater amplitude than the continuous bumps to offer the same benefit, leading to increased separation downstream of the bump position. The continuous bumps tested offered greater benefit, and therefore only results using the 'continuous' bump geometry approach are presented here.

Optimisation method

In this work the Multi-point Approximation Method MAM [27] [28] is used for the optimisation studies. It is a gradient based method that uses localised Design of Experiments (DoE) and trust regions to efficiently search through the design space. When using MAM, an initial generation of simulations (chosen by DoE) is carried out around the start point. A response surface is constructed for this region and the sub-optimal point found. The search is then moved to this point, where a new generation is constructed and the process repeated until the search converges on the optimal design. The MAM method has been shown to be an efficient and consistent approach for a wide range of highly-constrained optimisation problems, working successfully for design spaces made up of hundreds of parameters.

ROTOR 37 BUMP OPTIMISATION

For the Rotor 37 optimisation, the bump geometry was controlled at 5 radial heights (to allow radial variation of the parameters) with the geometry smoothly interpolated between the control stations using a cubic B-spline. The start and end points of the bumps were allowed to vary as shown in Table 1. Towards the tip the bump placement and movement range are increased in chord-wise position as the shock is sat further downstream at the tip. The initial design used at the start of the optimisation process had bumps positioned with approximately 60% of the bump downstream of the datum shock, as is known to be beneficial from previous work [10]. The objective function for the optimisation was blade efficiency and the simulations were carried out at 98% simulated choke.

The optimisations were carried out on the Rolls-Royce CFMS cluster using the MAM method. The geometry of the optimised shock bump can be seen in Figure 20. A slice at 60% span is shown. The 3D geometry compared to the datum is shown in Figure 21.

The bump applied to the datum geometry varies radially, with the maximum bump amplitude and width localised between 40 and 60% span. This makes sense as the strongest shock location, largest separation and maximum adjoint sensitivity occur around mid-span for Rotor 37, and therefore greater shock con-

TABLE 1: ROTOR 37 BUMP PARAMETER RANGES

Spanwise bump position	Min start point / chord	Max start point / chord	Min end point / chord	Max end point / chord
0-0.6	0.25	0.55	0.55	0.85
0.8	0.25	0.59	0.59	0.9
1.0	0.25	0.63	0.63	0.9

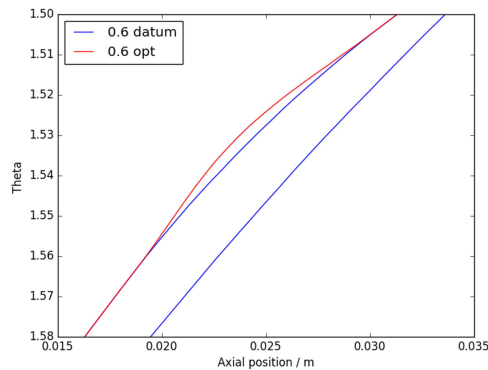


FIGURE 20: A SPANWISE SLICE OF THE DATUM AND OPTIMISED R37 GEOMETRIES AT 60% SPAN.



FIGURE 21: OPTIMISED R37 BUMP (BLUE) ADDED TO THE DATUM BLADE GEOMETRY (GREY)

control is needed in this region. The resulting variation from hub to tip of the geometry demonstrates the benefit provided by optimising the geometry. Without optimisation it would be difficult to manually specify the bump position, width, amplitude and asymmetry, which would result in reduced benefit.

Analysis of the R37 optimised bump design

The flow features for the resulting, optimised, continuous bump design is compared to the datum in Figure 22. The datum shock position is shown via a white line on the optimised geometry. It can be seen how the use of bumps has delayed the shock. The reduction in separation for the optimised design can be seen in Figure 23. The delay of the shock position has reduced the separation initiation point and the volume of separated flow.

The performance of this geometry is compared to the best individual bumps geometry (not described in detail here) and the datum in Table 2. It can be seen that the efficiency benefit is greatest for the continuous bump design. The efficiency is increased by 1.48%, while the pressure ratio is also increased. A summary of previous optimisation results for Rotor 37 by various researchers is given by John et al. [4]. The maximum efficiency benefit achieved by those studies was around 1.7-1.9% (without decreasing PR). These optimisations were able to modify parameters such as blade camber, thickness, lean and sweep though, so had greater design flexibility than the current shaping approach. This shows that the efficiency benefit provided through the application of shock control bumps is significant, considering the only geometry change is the addition of bumps.

TABLE 2: ROTOR 37 OPTIMISED BUMP PERFORMANCE COMPARISON.

	PR	Delta PR / %	Efficiency / %	Delta efficiency / %
Datum	2.05		85.45	
Individual	2.06	0.51	86.21	0.76
Cont.	2.08	1.2	86.93	1.48

Figure 24 shows the passage flow for the datum and optimised geometries at 50% span. The effect of the bump delaying the shock can be seen, with the datum shock position shown by the black line. The shock has been delayed by over 12% chord at this height. Just upstream of the shock the Mach number contour is lower, suggesting pre-compression has occurred. The boundary layer separation that forms the wake, highlighted by the dark blue, low velocity region, has reduced in width by 26% at the trailing edge for the optimised design.

Figure 25 shows the datum and optimised lift plots. It can be seen how the shock has been delayed. The C_p increases just upstream of the shock, showing that the bump has carried out pre-compression. The jump in pressure across the shock is also lower for the optimised design than for the datum, indicating it

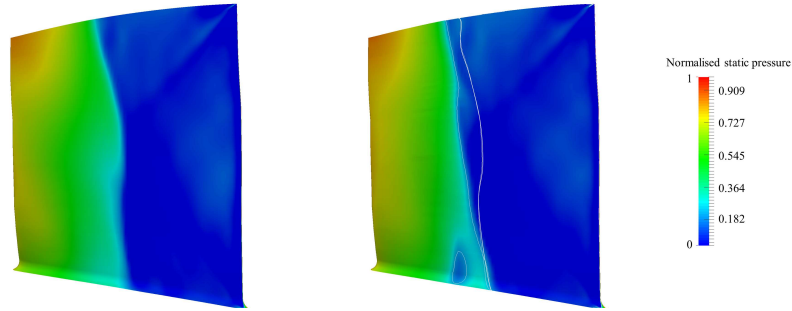


FIGURE 22: DATUM (LEFT) AND OPTIMISED (RIGHT) ROTOR 37 STATIC PRESSURE CONTOURS. FLOW DIRECTION RIGHT TO LEFT.

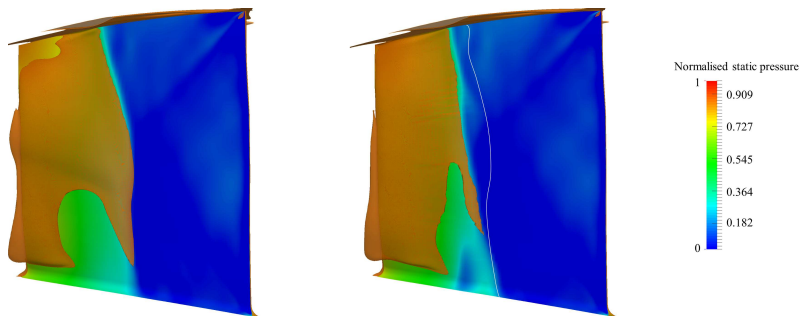


FIGURE 23: DATUM (LEFT) AND OPTIMISED (RIGHT) ROTOR 37 SEPARATED FLOW CONTOURS (ORANGE). FLOW DIRECTION RIGHT TO LEFT.

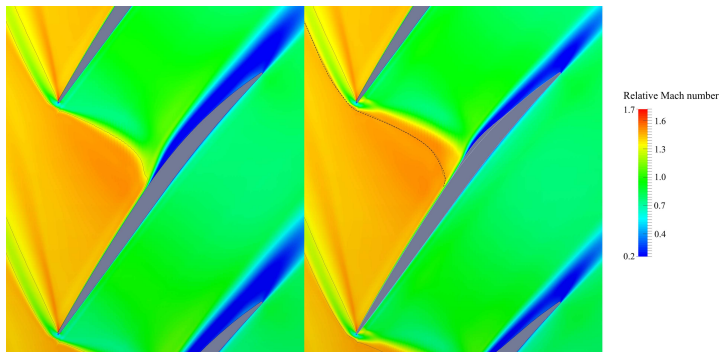


FIGURE 24: DATUM (LEFT) AND R37 OPTIMISED (RIGHT) FLOW FEATURES AT 50% SPAN.

has been weakened. Because the shock is delayed, it has become swallowed by the passage, causing an acceleration near to the leading edge on the blade pressure surface. This can be seen in the lower surface spike on the lift plot.

Performance across the characteristic for R37

The off-design performance is a key feature of blade aerodynamics. The characteristics for the datum and optimised designs

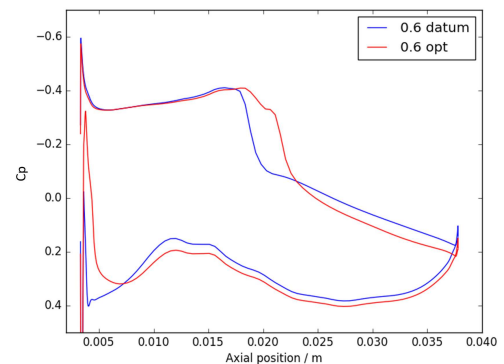


FIGURE 25: LIFT PLOTS FOR THE DATUM AND OPTIMISED GEOMETRIES AT 60% SPAN

are shown in Figure 26. An efficiency and pressure ratio increase has been achieved across the characteristic. The choke mass flow does not appear affected, although it is possible that the choke margin has been modified at other rotor speeds due to the throat area being reduced by the bump. The simulation results suggest a reduction in stall margin for the optimised design. This is due to the shock bump being mis-placed at conditions away from where

it was designed, leading to increased separation and thus reduced stall margin.

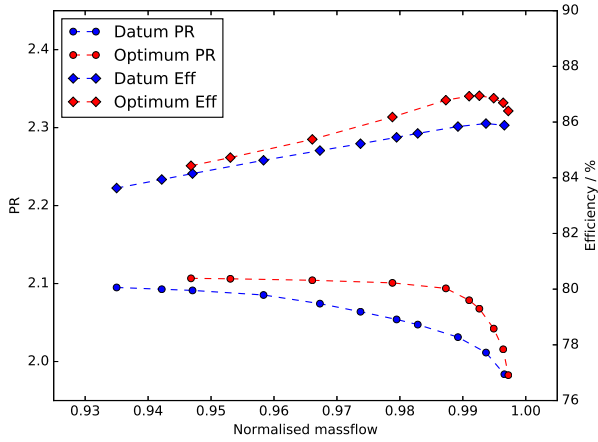


FIGURE 26: R37 OPTIMISED CHARACTERISTIC VS DATUM.

This section has demonstrated the benefit that can be achieved by applying shock control bumps to a compressor blade without modifying the entire blade geometry. This shows that a significant benefit is possible through geometry modifications via bumps just in the shock region.

RR-FAN BUMP OPTIMISATION

The benefit that shock control can provide in extending the stall margin of the RR-FAN case is investigated here. As described previously, an operating point on the stall side of the characteristic (point D) was selected for this analysis. The suction surface static pressure contour at this operating point is shown in Figure 27 to highlight the shock location. The region within which the bumps are to be added is highlighted and also listed in Table 3.

The optimisation was carried out using the MAM optimiser at condition D shown in Figure 15. The objective function is the blade efficiency, with the expectation that improving the efficiency at this near-stall point (by reducing separation) will improve the near-stall flow behaviour and stall margin. The effect of the resulting geometry on the separation is shown in Figure 28.

It can be seen that the bumps significantly reduce the shock induced separation, almost eliminating it. Towards the tip, a small separation region is present. This is likely due to the optimiser reaching a local minima and not finding a globally op-

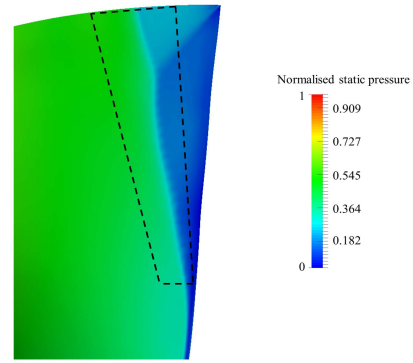


FIGURE 27: STATIC PRESSURE CONTOUR ON THE RR-FAN SUCTION SURFACE AND THE REGION WITHIN WHICH BUMPS ARE POSITIONED.

TABLE 3: RR-FAN BUMP PARAMETER RANGES.

Spanwise bump position	Min start point / chord	Max start point / chord	Min end point / chord	Max end point / chord
0.5	0	0.1	0.1	0.25
0.6	0	0.15	0.15	0.3
0.7	0.05	0.22	0.22	0.4
0.8	0.1	0.25	0.25	0.5
0.9	0.1	0.25	0.25	0.5
1.0	0.15	0.36	0.36	0.6

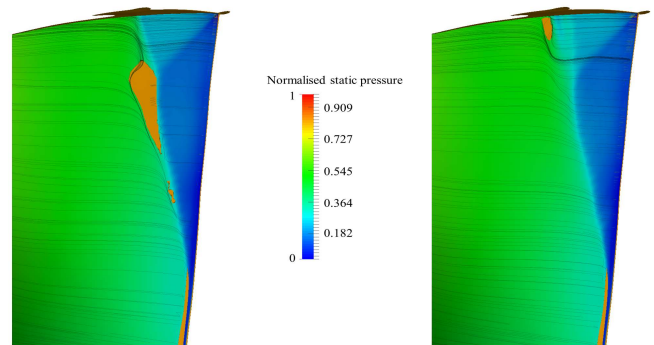


FIGURE 28: THE DATUM (LEFT) AND OPTIMISED RR-FAN (RIGHT) GEOMETRIES AT POINT D, WITH SEPARATION SHOWN IN ORANGE. FLOW DIRECTION RIGHT TO LEFT.

timum design. This is one of the limitations of gradient-based optimisation methods.

Figure 29 shows slices at 80% span of the datum and optimised RR-FAN bump geometries. It can be seen how the addition of the bump has weakened the contours across the shock, and reduced the dark blue, low-momentum regions of the boundary layer, separation and wake. The zoomed views show the geometry with bump compared to the datum. The bump geometry controls the shock and reduces the separation at the shock impingement point.

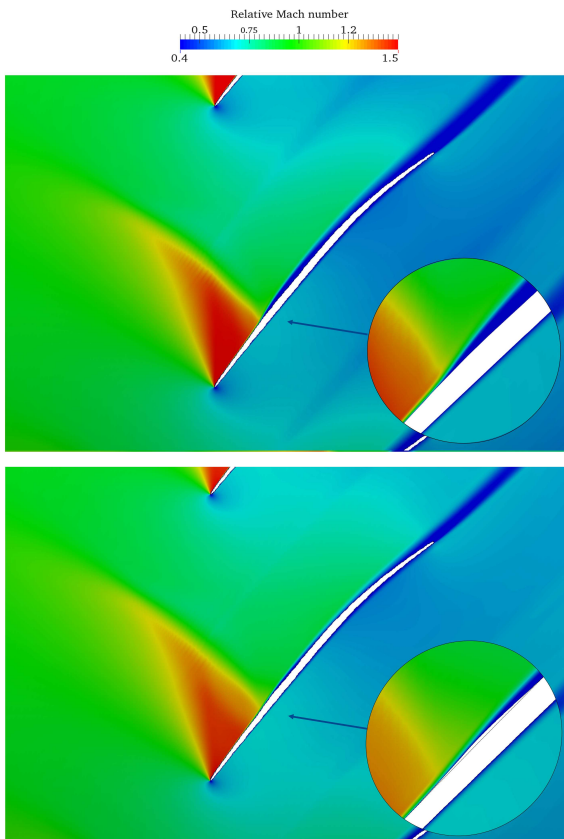


FIGURE 29: RELATIVE MACH NUMBER CONTOURS AT 80% SPAN (AT OPERATING POINT D), SHOWING THE DATUM (TOP) AND OPTIMISED RR-FAN (BOTTOM) GEOMETRIES.

Figure 30 shows how the wake of the blade at this height (measured downstream of the TE) has been reduced in width, by over 15%. The maximum relative Mach number deficit has also been reduced. The result is that the optimised design has lower loss generation due to the separation and wake, increasing its efficiency. This can be seen in Figure 32.

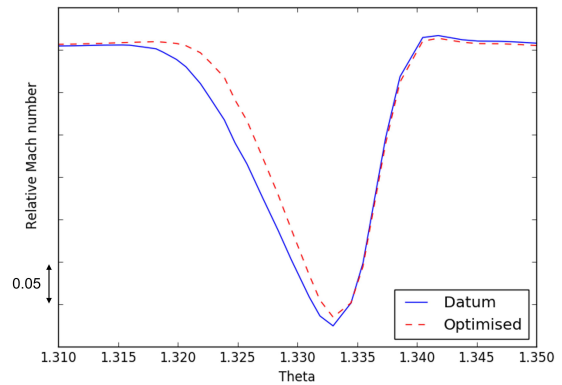


FIGURE 30: BLADE WAKES FOR THE DATUM AND OPTIMISED GEOMETRIES MEASURED AT 80% SPAN AND 0.1 CHORD DOWNSTREAM OF THE TRAILING EDGE.

Analysis of the stall margin and characteristic for RR-FAN

The application of shock control bumps has been shown to reduce shock induced separation at the near-stall condition (at which the optimisation was carried out). The objective for this case was to increase the stall margin via the use of these bumps. To assess whether this has been achieved, the optimum design was simulated at a variety of flow rates. The variation in blade behaviour at a range of flow rates near to stall is shown in Figure 31. It can be seen that the size of the separation is reduced at each of these operating points for the optimised design.

As shown in Figure 32, the presence of the bump allows an operating point on the left of the characteristic to remain unstalled, whereas full stall occurred at this point for the datum geometry. The bump designs reduce separation and delay the point at which the blade stalls. The impact of the added bumps for the rest of the fan operating range must also be assessed however.

As can be seen, the design has increased efficiency, and also stall margin at the left of the characteristic (the last stable point is further to the left for the optimised design), but unfortunately in doing so has adversely affected the behaviour nearer to the design point.

The bump that is designed to operate successfully near to stall results in unwanted flow behaviour at other flow rates. As the shock position moves (as the flow rate varies), the bump is no longer well aligned with the shock and has a negative impact. This effect can be seen in Figure 33 on the choke side of the characteristic. The bump causes a region of extra acceleration resulting in a stronger passage shock compared to the datum geometry. This increases entropy generation and results in lower efficiency on the right hand side of the characteristic. The flow capacity on the choke side of the characteristic is also affected (as can be seen in Figure 32) due to the impact of the bump at this flow rate.

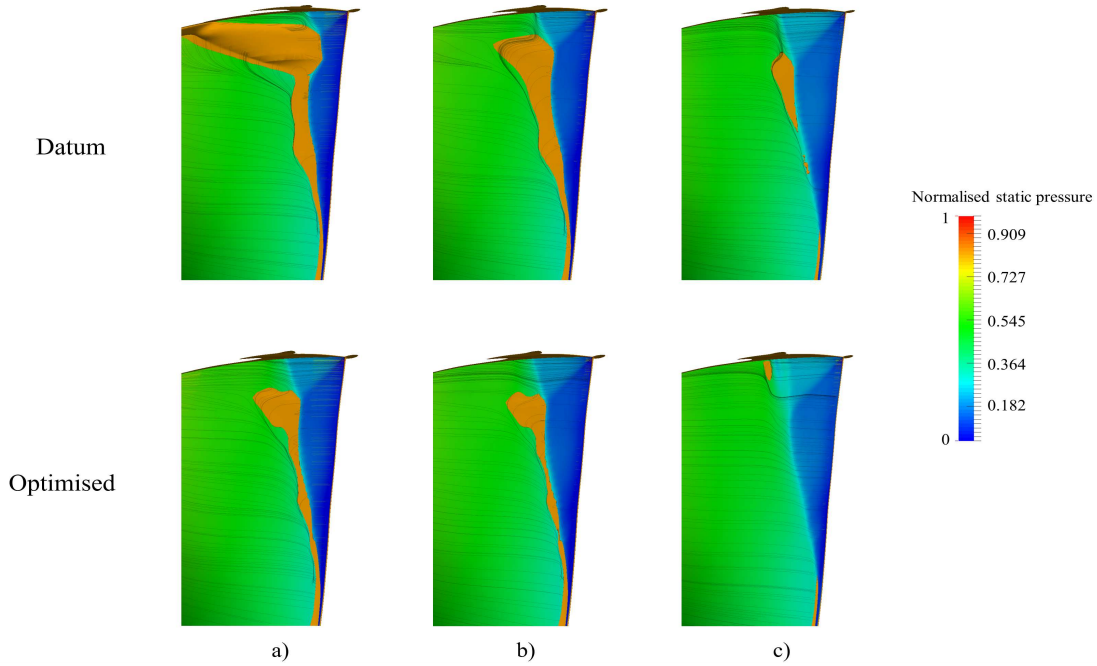


FIGURE 31: FLOW SEPARATION NEAR STALL FOR THE DATUM AND OPTIMISED RR-FAN DESIGNS AT a) B, b) C AND c) D OPERATING CONDITIONS. FLOW DIRECTION RIGHT TO LEFT.

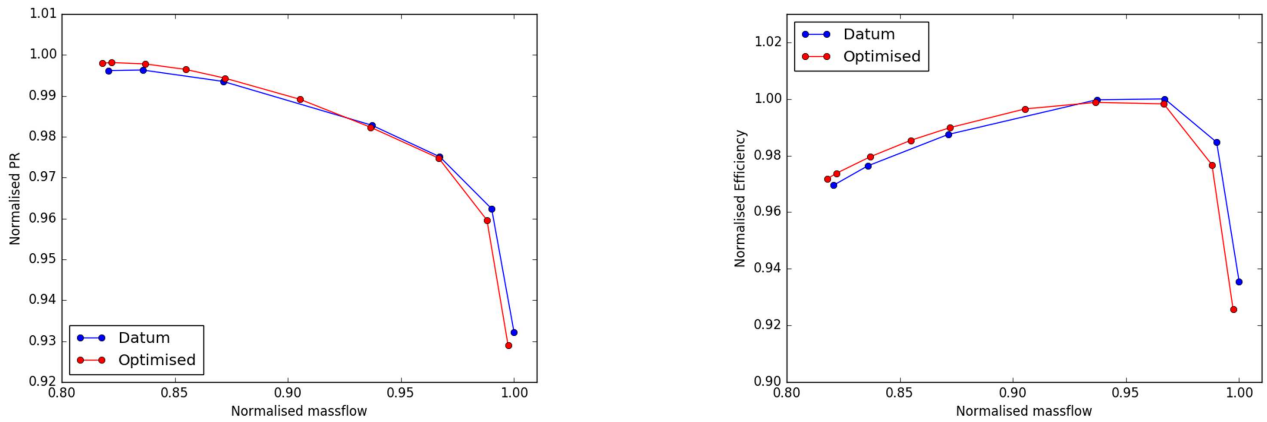


FIGURE 32: PR AND EFFICIENCY CHARACTERISTICS FOR THE DATUM AND OPTIMISED GEOMETRIES.

To assess whether further benefit in the near stall region could be achieved, the optimisation process was repeated at point B on the RR-FAN characteristic. This point is far closer to stall for the datum geometry, and as a result, the optimised design produced outperformed the datum and previous optimised design in the stall region. This can be seen in Figure 34. As occurred previously however, improving the performance in the stall region had a negative impact nearer to the design point. The choke

mass flow rate is reduced, and also the efficiency, for points on the right hand side of the characteristic compared to the datum. This highlights the impact that the optimisation design point has on the resulting design behaviour.

It must be noted that assessing the impact of these designs on fan stall margin using steady-state analysis has limitations, due to the truly unsteady nature of stall-inception. It has been demonstrated here that the application of shock control bumps

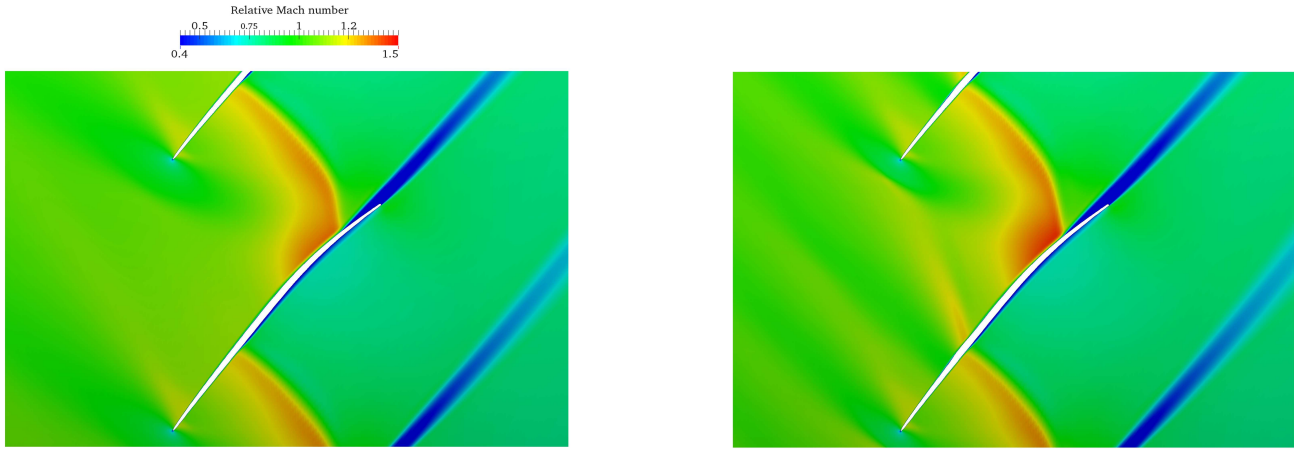


FIGURE 33: RELATIVE MACH NUMBER CONTOURS AT 80% SPAN (AT OPERATING POINT H), SHOWING THE DATUM (LEFT) AND OPTIMISED RR-FAN (RIGHT) GEOMETRIES.

can reduce the separation that appears to trigger fan stall. An assessment using unsteady simulations may be desirable to verify this benefit, but is beyond the scope of the current work.

CONCLUSION

This work has demonstrated how shock control bumps can be used to improve the performance of transonic fan/compressor blades. Blade geometries that incorporate shock control bumps have the ability to reduce shock loss and reduce/eliminate shock-induced separation and increase both efficiency and stall margin. Shock control bumps have the benefit that only small modifications to the blade geometry are required to achieve these improvements, compared to the large changes required by blade designs that make use of negative camber or similar shock control approaches. It has been demonstrated that both the efficiency and pressure ratio of a highly loaded compressor blade can be increased across a range of flow rates by delaying the shock and significantly reducing the separation and wake. For a modern fan blade the optimised bump design eliminated the majority of separation, reduced the thickness of the wake and extended the stall margin.

FUTURE WORK

To find improved benefit from the use of shock control bumps, a multi-point optimisation approach could be used, where the optimisation balances the performance between the design and off-design conditions. This would ensure that any benefit achieved at one point does not significantly deteriorate the performance elsewhere.

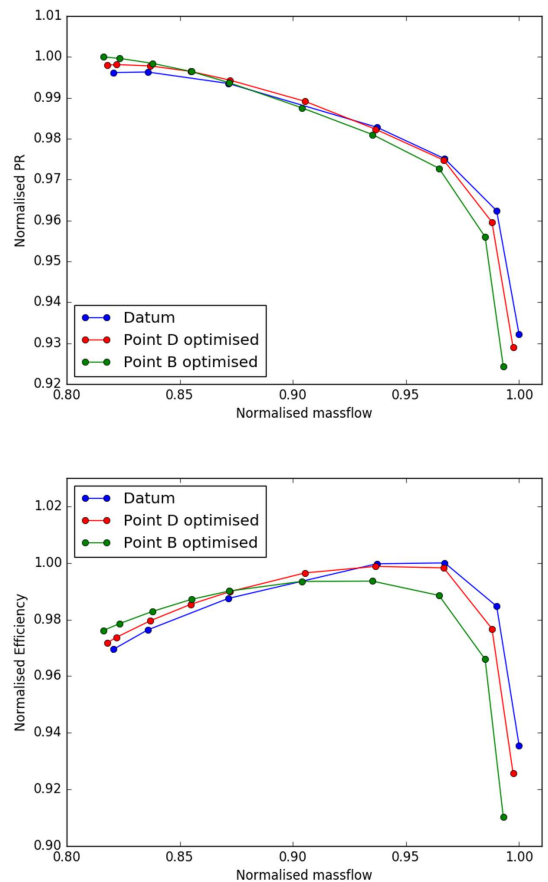


FIGURE 34: PR AND EFFICIENCY CHARACTERISTICS FOR THE DATUM, POINT D OPTIMISED AND POINT B OPTIMISED GEOMETRIES.

ACKNOWLEDGMENT

The first author is funded by a scholarship from the University of Sheffield. The authors would like to thank Rolls-Royce for their support and permission to publish the work.

REFERENCES

- [1] Ginder, R., and Calvert, W., 1987. “The design of an advanced civil fan rotor”. *Journal of turbomachinery*, **109**(3), pp. 340–345.
- [2] Cumpsty, N. A., 1989. *Compressor aerodynamics*. Longman Scientific & Technical.
- [3] Prince, D. C., 1980. “Three-dimensional shock structures for transonic/supersonic compressor rotors”. *Journal of Aircraft*, **17**(1), pp. 28–37.
- [4] John, A., Shahpar, S., and Qin, N., 2017. “Novel compressor blade shaping through a free-form method”. *Journal of Turbomachinery*, **139**(8), p. 081002.
- [5] Tai, T. C., 1977. Theoretical aspects of dromedaryfoil. Tech. rep., DTIC Document.
- [6] Ashill, P., and Fulker, J., 1992. “92-01-022 a novel technique for controlling shock strength of laminar-flow aerofoil sections”. *DGLR BERICHT*, pp. 175–175.
- [7] Drela, M., and Giles, M. B., 1987. “Viscous-inviscid analysis of transonic and low reynolds number airfoils”. *AIAA journal*, **25**(10), pp. 1347–1355.
- [8] Sommerer, A., Lutz, T., and Wagner, S., 2000. “Design of adaptive transonic airfoils by means of numerical optimisation”. In Proceedings of ECCOMAS, 2000, Barcelona.
- [9] Colliss, S. P., Babinsky, H., Nübler, K., and Lutz, T., 2016. “Vortical structures on three-dimensional shock control bumps”. *AIAA Journal*, pp. 2338–2350.
- [10] Stanewsky, E., 2002. *Drag Reduction by Shock and Boundary Layer Control: Results of the Project EUROSHOCK II. Supported by the European Union 1996-1999*, Vol. 80. Springer Science & Business Media.
- [11] Qin, N., Wong, W., and Le Moigne, A., 2008. “Three-dimensional contour bumps for transonic wing drag reduction”. *Proceedings of the Institution of Mechanical Engineers, Part G: Journal of Aerospace Engineering*, **222**(5), pp. 619–629.
- [12] Mazaheri, K., and Khatibirad, S., 2017. “Using a shock control bump to improve the performance of an axial compressor blade section”. *Shock Waves*, **27**(2), pp. 299–312.
- [13] Hicks, R. M., and Henne, P. A., 1978. “Wing design by numerical optimization”. *Journal of Aircraft*, **15**(7), pp. 407–412.
- [14] Suder, K. L., and Celestina, M. L., 1994. “Experimental and computational investigation of the tip clearance flow in a transonic axial compressor rotor”. In ASME 1994 International Gas Turbine and Aeroengine Congress and Exposition, no. 94-GT-365, American Society of Mechanical Engineers.
- [15] Reid, L., and Moore, R. D., 1978. “Performance of single-stage axial-flow transonic compressor with rotor and stator aspect ratios of 1.19 and 1.26, respectively, and with design pressure ratio of 1.82”. *NASA-TP-1659*.
- [16] Hah, C., 2009. “Large eddy simulation of transonic flow field in nasa rotor 37”. In 47th AIAA Aerospace Sciences Meeting including The New Horizons Forum and Aerospace Exposition, p. 1061.
- [17] Dunham, J., 1998. Cfd validation for propulsion system components (la validation cfd des organes des propulseurs). Tech. rep., DTIC Document.
- [18] Chima, R., 2009. “Swift code assessment for two similar transonic compressors”. In 47th AIAA Aerospace Sciences Meeting including The New Horizons Forum and Aerospace Exposition, p. 1058.
- [19] Denton, J., 1997. “Lessons from rotor 37”. *Journal of Thermal Science*, **6**(1), pp. 1–13.
- [20] Cumpsty, N., 2010. “Some lessons learned”. *Journal of turbomachinery*, **132**(4), p. 041018.
- [21] Seshadri, P., Parks, G. T., and Shahpar, S., 2014. “Leakage uncertainties in compressors: The case of rotor 37”. *Journal of Propulsion and Power*, **31**(1), pp. 456–466.
- [22] Lapworth, L., 2004. “Hydra-cfd: a framework for collaborative cfd development”. In International Conference on Scientific and Engineering Computation (IC-SEC), Singapore, June, Vol. 30.
- [23] Shahpar, S., and Lapworth, L., 2003. “Padram: Parametric design and rapid meshing system for turbomachinery optimisation”. In ASME Turbo Expo 2003, collocated with the 2003 International Joint Power Generation Conference, American Society of Mechanical Engineers, pp. 579–590.
- [24] John, A., Qin, N., and Shahpar, S. “The impact of realistic casing geometries and clearances on fan blade tip aerodynamics (gt2017-64403)”. *Journal of Turbomachinery*.
- [25] Duta, M. C., Shahpar, S., and Giles, M. B., 2007. “Turbomachinery design optimization using automatic differentiated adjoint code”. In ASME Turbo Expo 2007: Power for Land, Sea, and Air, American Society of Mechanical Engineers, pp. 1435–1444.
- [26] Kulfan, B. M., Bussoletti, J. E., et al., 2006. “Fundamental parametric geometry representations for aircraft component shapes”. In 11th AIAA/ISSMO multidisciplinary analysis and optimization conference, Vol. 1, sn, pp. 547–591.
- [27] Toropov, V., va, F., Markine, V., and d, H., 1996. “Refinements in the multi-point approximation method to reduce the effects of noisy structural responses”. In 6th Symposium on Multidisciplinary Analysis and Optimization, p. 4087.
- [28] Polynkin, A., Toropov, V., and Shahpar, S., 2008. “Adaptive and parallel capabilities in the multipoint approxima-

tion method”. In 12th AIAA-ISSMO MDO Conference, Victoria, British Columbia, Canada, September, pp. 10–12.